



OPEN

SUBJECT AREAS:
IMAGING AND SENSING
THREE-DIMENSIONAL IMAGINGReceived
19 February 2014Accepted
3 July 2014Published
30 July 2014Correspondence and
requests for materials
should be addressed to
D.R. (dr@tum.de)

Functional optoacoustic imaging of moving objects using microsecond-delay acquisition of multispectral three-dimensional tomographic data

Xosé Luís Deán-Ben¹, Erwin Bay¹ & Daniel Razansky^{1,2}¹Institute for Biological and Medical Imaging (IBMI), Helmholtz Center Munich, Ingolstädter Landstraße 1, 85764 Neuherberg, Germany, ²Faculty of Medicine, Technical University of Munich, Ismaninger Straße 22, 81675 Munich, Germany.

The breakthrough capacity of optoacoustics for three-dimensional visualization of dynamic events in real time has been recently showcased. Yet, efficient spectral unmixing for functional imaging of entire volumetric regions is significantly challenged by motion artifacts in concurrent acquisitions at multiple wavelengths. Here, we introduce a method for simultaneous acquisition of multispectral volumetric datasets by introducing a microsecond-level delay between excitation laser pulses at different wavelengths. Robust performance is demonstrated by real-time volumetric visualization of functional blood parameters in human vasculature with a handheld matrix array optoacoustic probe. This approach can avert image artifacts imposed by velocities greater than 2 m/s, thus, does not only facilitate imaging influenced by respiratory, cardiac or other intrinsic fast movements in living tissues, but can achieve artifact-free imaging in the presence of more significant motion, e.g. abrupt displacements during handheld-mode operation in a clinical environment.

First optoacoustic images from living biological tissues were demonstrated over a decade ago^{1,2}. The unique advantages of this hybrid imaging technology drive continuous technical advancements as well as its use in a number of novel biomedical applications. In optoacoustics, sound waves are induced by absorption of time-variant light radiation³, which allows for high-resolution imaging of rich optical contrast beyond the depth-penetration limits imposed by light scattering. Thus, otherwise unresolvable or undetectable anatomy and function can now be visualized at millimeter to centimeter scale depths in living organisms^{4,5}.

Translation into clinical practice occurs to be the natural next step so that the unique strengths offered by the optoacoustic technology can be fully exploited. Several dedicated systems using endoscopic, hand-held, or stationary design approaches have been recently proposed for clinical use, with multiple applications envisioned in diagnosis of breast cancer^{6,7} and cardiovascular disease⁸, ocular imaging⁹, visualization of arthritis¹⁰, lymphatic system¹¹, skin abnormalities¹², prostate¹³ and thyroid glands¹⁴. Of particular convenience is the use of hand-held probes, which permits real-time visualization of dynamic events, and has the potential to speed up clinical examinations on a broad range of applications. In fact, these are also the main assets that propelled ultrasonography into the most-widely-employed imaging modality in today's clinical practice. On the other hand, the optoacoustic tomographic reconstruction problem and physics behind the signal excitation substantially differ from ultrasonography. While linear arrays are typically used in ultrasound imaging, curved array geometries proved to be a significantly better strategy for collection of optoacoustic responses and further resulted in more accurate reconstructions^{15,16}. Moreover, optoacoustic excitation via laser light offers additional exclusive capacities, such as intrinsic ability to acquire full tomographic datasets within a single interrogation laser pulse, thus achieving real-time three-dimensional imaging capacity^{17–19}. Most importantly, by acquisition of images at multiple optical wavelengths, multispectral optoacoustic tomography (MSOT) can map functional contrast as well as the bio-distribution of molecular agents in tissues^{20,21}.

Real-time acquisition of multispectral datasets imposes significant technological challenges when considering motion in living subjects, e.g. due to breathing or heartbeat. Even more significant artifacts may be introduced by operating optoacoustic imaging devices in a hand-held mode. Several prior attempts to avoid motion-related artifacts in multispectral optoacoustic imaging were done using high repetition lasers in optoacoustic endoscopy²²



and optical-resolution photoacoustic microscopy²³, as well as by means of Raman shifters in acoustic resolution optoacoustic microscopy²⁴. Yet, these implementations employ a single detector approach, which only renders real-time performance in two dimensions and is overall not suitable for hand-held operation. Most recently, a true five-dimensional (5D) optoacoustic tomographic approach has been demonstrated by fast laser wavelength tuning and real-time acquisition and visualization of three-dimensional multispectral data using spherical matrix array detection geometry²⁵. Yet, the substantial (millisecond level) time delay between the excitation laser pulses at different wavelengths has severely limited the application in hand-held mode. Significant motion artifacts introduced by hand-held scanning were observed when the velocity of the probe exceeded several mm/s. The displacement d of the probe between consecutive laser pulses is given by $d = v/\text{PRF}$, where v is the scanning velocity and PRF is the pulse repetition frequency of the laser. For instance, considering a pulse repetition frequency of 50 Hz and a relatively slow hand-held scanning velocity of 5 mm/s, the probe moves by 100 μm between two consecutive pulses at two different wavelengths, which prevents accurate spectral unmixing preserving high spatial resolution. Motion effects scale with the number of wavelengths used for multispectral data acquisition, further affecting the accuracy of real-time multispectral imaging.

In this work, we explore the feasibility of functional volumetric (three-dimensional) optoacoustic imaging in a hand-held mode by introducing a microsecond-range (as opposed to millisecond-range) delay between laser pulses at different wavelengths. In this way, the time lapse required for collection of multispectral data can be minimized, eliminating potential motion artifacts and enabling functional multispectral imaging even during the presence of abrupt displacements of the imaging probe.

Results

Experimental concept. The layout of the experimental system employed is depicted in Fig. 1. Acquisition of three-dimensional tomographic data in real time was performed by an optoacoustic hand-held probe consisting of an ultrasound array with 256 piezoelectric elements distributed on a spherical surface²⁶. Details on the array geometry are provided in the methods section. Optoacoustic responses in the imaged object are excited by nanosecond-duration pulsed beams from two tunable OPO lasers (Phocus, Oportek Inc., Carlsbad, CA), which were set at wavelengths of 760 nm and 850 nm. The light was guided through a custom-made fiber bundle (CeramOptec GmbH, Bonn, Germany) having two input arms and a common output arm. The individual fibers at the output of the bundle were randomly distributed with respect to the two inputs so that both beams created approximately the same illumination profile at the tissue surface. The first laser was internally triggered whereas the flash lamps and Q-switch of the second laser were externally triggered and conveniently delayed as shown in Fig. 2a. Two delay generators were used in the synchronization scheme. The first delay D_1 was selected according to $D_1 = T - L$ from the Q-switch output of the first laser, where T and L denote the pulse interval and the resulting time lapse between the two laser pulses, respectively. Since both corresponding time-resolved signals were detected within the same acquisition window, the time lapse L needs to be sufficiently long to separate the reconstructed images. Given a pulse interval of $T = 100$ ms, a value of 99.983 ms was chosen for D_1 which translates into a time lapse of $L = 17$ μs between the Q-Switch trigger signals of the two lasers. This time lapse corresponds to approximately 26 mm of propagation of the ultrasound wave within tissue, which is larger than the imaged region of interest, thus no crosstalk between two consecutive images acquired at the two wavelengths is expected. Since the second laser is triggered externally, both Q-Switch and flash lamps needed to be synchronized. To ensure optimal signal energy, a delay of $C = 180$ μs

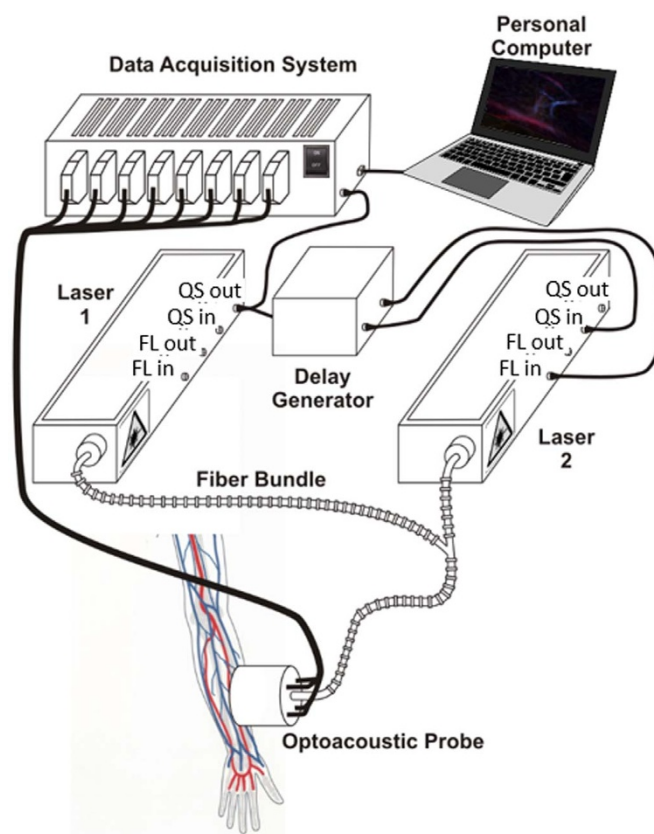


Figure 1 | Lay-out of the experimental set-up. The computer picture was developed by the authors. QS-Q-switch, FL-flash lamp.

had to be set between the respective trigger signals. This was maintained by setting the delay of the second delay generator D_2 to a value of 99.820 ms from the Q-switch input of the second laser according to $D_2 = T - C$.

Imaging of tissue vasculature in a healthy volunteer. The palm of a healthy volunteer was scanned in order to test the *in-vivo* imaging performance of the introduced method. An example of optoacoustic signals acquired from two microsecond-delayed laser pulses is displayed in Fig. 2b. It can be seen that the optoacoustic responses due to pulses at two different wavelengths can be separated on a time axis without cross talk. Yet, the short delay of only 17 μs between the two pulses ensured that no motion artifacts affect the unmixing of the multi-spectral data. The imaging results are showcased in Fig. 3 while two additional movie files are available in the online version of the manuscript that best illustrate the attained imaging performance in a dynamic fashion. Image reconstruction and unmixing was performed as described in the methods section. Figs. 3a and 3b display examples of maximum intensity projection (MIP) images acquired respectively at 760 nm and 850 nm, both color-coded for depth. For the same imaged volume, images acquired at 850 nm show a different appearance than those at 760 nm, which is mostly related to the strong wavelength-dependent absorption by the blood chromophores. For instance, the highly oxygenated vessels (arteries) are naturally expected to present higher signal intensities for the 850 nm wavelength as compared to 760 nm, whereas an opposite effect is expected for less oxygenated vessels (veins). The distinction between vessels with different blood oxygenation levels is best perceived in the blood oxygen saturation maps displayed in Fig. 3c. One should notice that wavelength-dependent light attenuation may lead to uncertainties (errors) in estimating the blood oxygen saturation, which also scale with depth. Our analysis, based on the procedure detailed in the methods section, reveals that for vessels

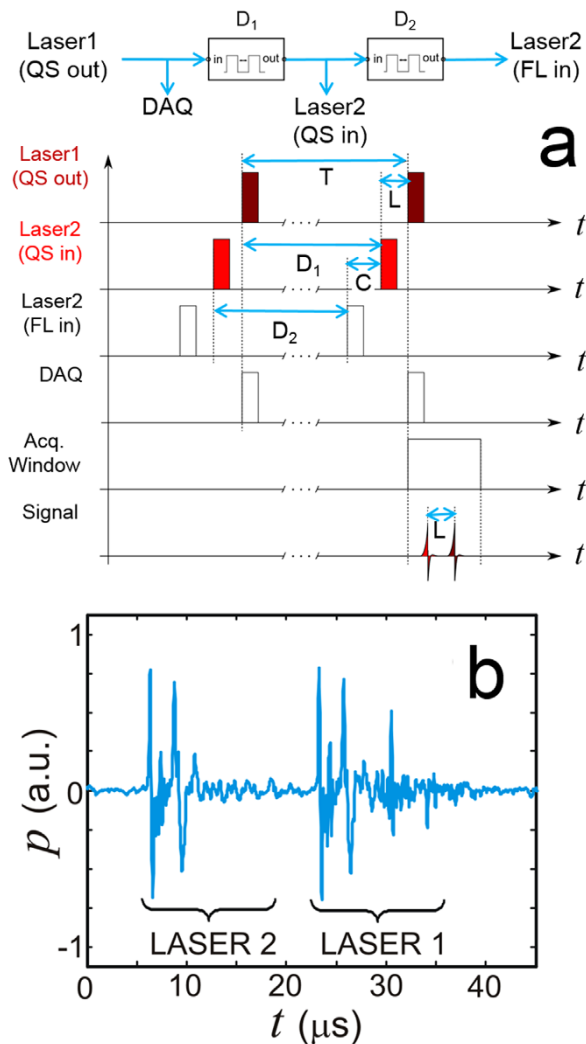


Figure 2 | (a) Synchronization scheme between the two lasers. (b) Example of the typically acquired optoacoustic signal train. QS – Q-switch, FL – flash lamp, DAQ – data acquisition system.

shallower than 6 mm (as shown in Fig. 3), such uncertainty is generally expected to be lower than 15% (Fig. 4). However, significant errors may be introduced at deeper locations and a model accounting for the effects of light attenuation in tissues is needed for accurate estimation of the oxygen saturation. The dynamic imaging capacity is further showcased in the two movie files available in the online version of the journal. In this case, the MIPs of the unmixed distribution of oxygenated and deoxygenated hemoglobin are displayed in arbitrary units in all three axes for better distinction of vessels having different oxygen saturation levels. Movie 1 demonstrates the ability to resolve distribution of oxygenated and deoxygenated hemoglobin in a pulsating artery from the data captured by the resting hand-held probe system. In Movie 2 the system is shown to attain dynamic tracking of deep human vasculature in real time by moving the handheld probe along the skin surface. In both cases, no motion artifacts were detected in the images corresponding to the different wavelengths, so that fast acquisition of multispectral datasets enables generation of motion-artifact-free functional images.

Comparison to the fast wavelength tuning approach. To compare the performance of the suggested method to the fast wavelength tuning approach, we simulated the latter by using instead the multispectral data from two adjacent laser pulses separated by

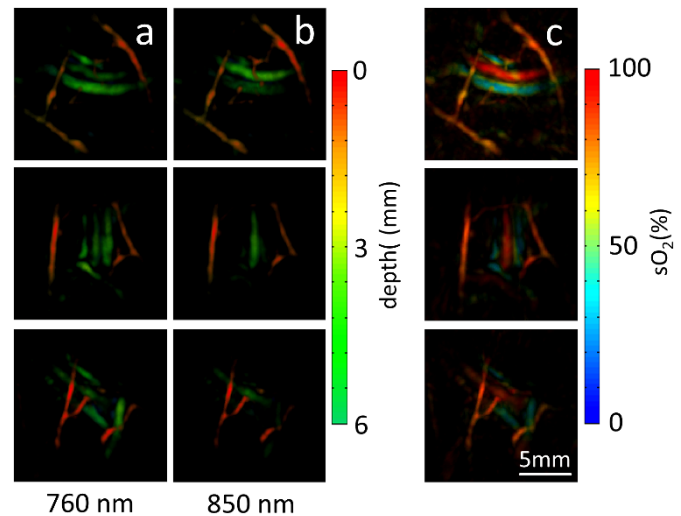


Figure 3 | Optoacoustic images of tissue vasculature in a healthy volunteer acquired using the three-dimensional handheld probe and the developed microsecond delay approach. (a) Volumetric images at 760 nm color-coded for depth. (b) The corresponding images at 850 nm. (c) Blood oxygen saturation maps (maximum intensity projections along the depth direction) derived by spectral unmixing of the multispectral data. The scalebar corresponds to 5 mm.

approximately 100 ms. The reconstructed MIP representations of the volumetric images acquired at 760 nm and 850 nm using both methods are compared in Fig. 5. A manual (feature-based) motion correction of the images at the two wavelengths has been further performed for the simulated fast wavelength tuning approach. Motion-related errors were not identified in images acquired using the microsecond-delay data (panels a–c). However, motion-related errors were prominent in images acquired with the fast wavelength tuning approach (panels d–f). The motion between images can be best recognized when superimposing the images at 760 nm onto the respective images at 850 nm (see the green squares in Figs. 5b and 5e). Clearly, when the two images are separated in time by 100 ms, the structures are shifted by approximately 800 μm between adjacent pulses at the two different wavelengths, making spectral unmixing an impossible task during even a relatively slow scanning speed of 8 mm/s. Manual correction for motion before performing the unmixing step is still not able to rectify all the motion-related artifacts in the unmixed images (Fig. 5f). For example, the vessel marked ‘A’ obviously generates similar signal intensities at the two wavelengths when the data is acquired using the microsecond-delay approach (Figs. 5a and 5b), whereas the same vessel generates a stronger signal level at 760 nm versus 850 nm when the acquisition at the two wavelengths is separated by ~ 100 ms (Figs. 5d and 5e). This discrepancy can be attributed to a shift in the light fluence and sensitivity maps of the detection array as it moves to a slightly different location. As a result, unmixing of motion-affected data would give rise to erroneous interpretation of low oxygen saturation in the vessel (Fig. 5f versus Fig. 5c). The opposite effect occurs for the vessel marked ‘B’, which appears to generate much stronger signal intensity at 850 nm due to motion. As a result, the blood oxygen saturation in this particular vessel is overestimated.

Discussion

The results demonstrate the feasibility of three-dimensional real-time functional imaging free of motion-related artifacts. The presented approach was demonstrated to successfully mitigate artifacts in the presence of intrinsic tissue motion, such as circulation or respiratory movements, but also when fast scanning with a handheld probe is performed. For the dual wavelength approach used in the

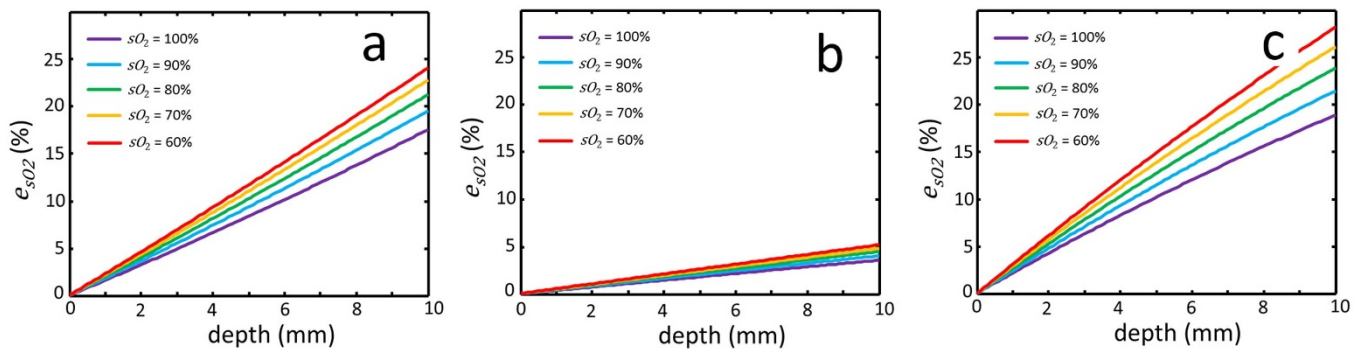


Figure 4 | Uncertainty (error) in approximating the blood oxygen saturation $s_{O_2,a}$ of a target point located at different depths by assuming wavelength independent light fluence $\bar{\phi}(r)$ in Eq. (2). Three different oxygen saturation values of the background tissues $s_{O_2,b}$ are considered, namely 90% (a), 70% (b) and 50% (c).

current study, even moving the probe at unreasonably high velocity of 2 m/s with respect to the imaged object would only result in displacement of 34 μm within the 17 μs delay between laser pulses at the two wavelengths, which is below the achievable spatial resolution of the three dimensional imaging probe. Furthermore, using the proposed method, hand-held scanning can be performed with low laser repetition rate of several tens of pulses per second allowing for high per-pulse energies in the tens and hundreds millijoule range that still conform to laser safety standards, thus guaranteeing good signal-to-noise performance and deep tissue penetration. For comparison, in order to reduce motion artifacts in conventional multispectral optoacoustic tomography using a single laser source, the repetition rate of the laser must be significantly increased in order to achieve fast wavelength tuning and minimize the time lapse between pulses at different wavelengths²⁵. However, this would not constitute a viable alternative to the approach suggested here since increasing the pulse repetition rate would readily imply corresponding reduction of the per-pulse energies in order to conform to the laser safety standards on the average light intensities delivered to the imaged subject²⁷. Decreasing the per-pulse energy would come at the adverse

compromise of reduced signal-to-noise levels and imaging penetration into tissue.

Clearly, the presented approach requires the use of two or more laser sources, depending on the number of acquired wavelengths. This comes at the expense of a higher implementation cost and more design complexity of the data acquisition system and synchronization electronics. Thus, ideally, alternative methods shall be sought for generation of multiple pulses with microsecond delays. While generation of low energy pulses in the nanojoule and microjoule range with microsecond level delays is indeed possible using pulsed laser diodes^{28,29}, a different technology will be necessary to manufacture affordable devices for deep-tissue multispectral imaging with pulse energies in the tens of millijoules range.

In conclusion, it is anticipated that the presented functional three-dimensional optoacoustic imaging approach free of motion artifacts will further prompt introduction of the new groundbreaking capabilities of optoacoustic imaging into clinical practice.

Methods

Experimental setup. An optoacoustic hand-held probe based on matrix detection array was used to acquire three-dimensional tomographic data in real time²⁶. The array consists of 256 piezoelectric elements with a central frequency of 4 MHz and a bandwidth of ca. 100% (-6 dB), which are densely distributed over a spherical surface with a radius of 4 cm covering an angle of approximately 90° (solid angle of $2\pi[1 - \cos(\pi/4)]$). The three-dimensional imaging probe supports nearly isotropic spatial resolution of 200 μm in a volume of ca. 1 cm^3 surrounding the center of the sphere²⁶. The output arm of the fiber bundle is inserted into a cylindrical cavity with a diameter of 8 mm located in the center of the array to provide optical illumination along its central axis. Acoustic coupling to the imaged part is ensured with a water-containing transparent polyethylene membrane. Acoustic gel was further applied for optimal acoustic coupling between the skin of the imaged subject and the membrane. The pressure signals at the 256 locations of the array elements are simultaneously collected with a sampling frequency of 40 megasamples per second at 2030 instants, immediately following the trigger signal of the first laser pulse. A custom-designed data acquisition system (Falkenstein Mikrosysteme GmbH, Taufkirchen, Germany) is used for simultaneous digital sampling of the analog data from the 256 channels. The acquisition is triggered with the Q-switch output of the first laser, and the acquired signals are subsequently transmitted to a personal computer through a 1 Gbit Ethernet connection.

Image reconstruction and unmixing. It has been long recognized that extraction of quantified information from optoacoustic images is strongly conditioned by accuracy of the employed image reconstruction and spectral unmixing schemes³⁰. For image reconstruction in multispectral optoacoustic tomography, the acquired signals at each wavelength are first deconvolved with the electrical impulse response of the transducer and band-pass filtered between 0.2 and 7 MHz. An accurate model-based reconstruction algorithm³¹ is then applied to reconstruct the images for each wavelength. When properly reconstructed, the optoacoustic image $OA(r,\lambda)$, representing the pressure field generated by absorption of light energy at a certain wavelength λ , is proportional to the product of the optical absorption coefficient $\mu_a(r,\lambda)$, the light fluence $\phi(r,\lambda)$ and the dimensionless Grüneisen parameter $\Gamma(r)$. By further considering the optical absorption as superposition of contributions from the different absorbing substances present in tissue, $OA(r,\lambda)$ can be expressed as

$$OA(r,\lambda) = \Gamma(r)\phi(r,\lambda) \sum_i \epsilon_i(\lambda)C_i(r), \quad (1)$$

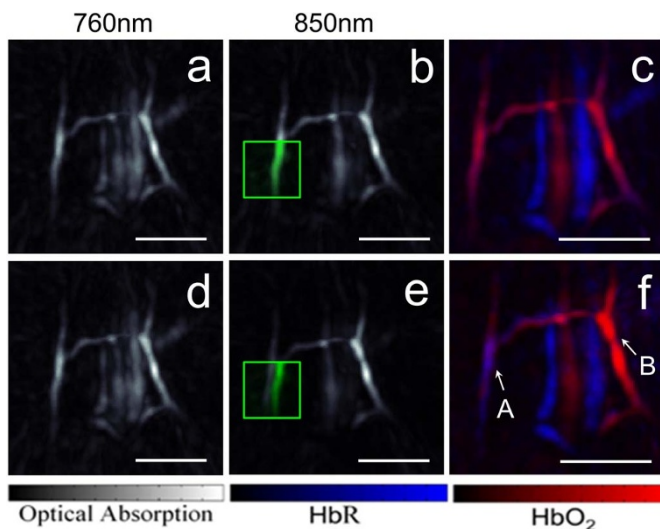


Figure 5 | Maximum intensity projections of the images acquired with two laser pulses separated by 17 μs (a–b) and the corresponding image representing the unmixed distributions of oxygenated and deoxygenated haemoglobin (c). The corresponding images acquired with two adjacent laser pulses separated by approximately 100 ms are shown in (d–f). Part of the image data in (a) and (d) is superimposed in green into the areas marked with the green squares in (b) and (e). Maximum intensity projections along the depth direction are shown. The scalebar corresponds to 5 mm.



where $\varepsilon_i(\lambda)$ and $C_i(r)$ are the molar extinction coefficient and the spatial distribution (concentration) of the individual absorbing substances. Assuming that the main tissue chromophores in the imaged wavelength range are oxygenated (HbO₂) and deoxygenated (HbR) hemoglobin and the main wavelength dependence arises from the extinction spectra of hemoglobin, Eq. (1) can be approximated as

$$OA(r, \lambda) \approx \Gamma(r) \bar{\phi}(r) [\varepsilon_{HbR}(\lambda) C_{HbR}(r) + \varepsilon_{HbO_2}(\lambda) C_{HbO_2}(r)], \quad (2)$$

where $\bar{\phi}(r)$ is the mean light fluence distribution for the wavelength range employed. In order to estimate the concentrations of the two chromophoric components, a spectral unmixing procedure based on a per-pixel least square fitting of the photoacoustic images at different wavelengths to a linear combination of molar extinction coefficients of oxygenated and deoxygenated hemoglobin is performed³². Subsequently, the spatial distribution of oxygen saturation is estimated via

$$sO_2(r) = \frac{C_{HbO_2}(r)}{C_{HbO_2}(r) + C_{HbR}(r)}. \quad (3)$$

Uncertainty in the oxygen saturation calculation. Since $sO_2(r)$ is calculated as a ratio, it is not directly influenced by quantitative errors in the reconstructed single-wavelength images. Nevertheless, the entire procedure relies on approximations made in deriving Eq. (2) so that inaccuracies are possibly introduced in cases of strong wavelength dependence of the light attenuation, e.g. when considering deep tissue imaging scenarios. Other factors causing significant spectral dependence of photoacoustic signals, such as wavelength-dependent illuminating beam profile, or presence of additional absorbers may all lead to further errors in the estimation of $C_{HbR}(r)$ and $C_{HbO_2}(r)$ via Eq. (2). One may estimate the expected inaccuracy of the blood oxygen saturation estimation due to wavelength dependence of the light attenuation using a recently published procedure³³. Since in our experiments the surface of the imaged object is illuminated with a broad light beam, a first-order assessment of the wavelength-dependent light fluence as a function of depth $\phi(r, \lambda)$ can be obtained with a one-dimensional light diffusion model considering a uniform background³³. Since the detected photoacoustic signals are normalized to the laser energy measured on a per-pulse basis, the light intensity at the air-tissue interface (semi-infinite medium) is assumed to be equal for both wavelengths. In calculating the wavelength dependent fluence, representative values of the background reduced scattering coefficient of $\mu_s'(\lambda) = 18.9(\lambda/500 \text{ nm})^{-1.286}$ and average blood concentration of 5.89 g/l in the forearm were assumed³⁴. The background optical absorption coefficient μ_a for both wavelengths is calculated for this average blood concentration and different oxygen saturation levels. Considering a spatially-independent Grüneisen parameter in soft tissues, the photoacoustically-generated signals in each image voxel can be calculated according to Eq. (1) for a given oxygen saturation sO_2 in the target voxel and a uniform oxygen saturation $sO_{2,b}$ in the background tissues. From the generated photoacoustic signals, the approximated oxygen saturation $sO_{2,a}$ in each voxels can be directly extracted via Eq. (2), which assumes the same light fluence distribution for both wavelengths. In this way, the expected error in the estimation of the oxygen saturation in the target voxel is given by

$$\varepsilon_{sO_2} = |sO_{2,a} - sO_2| \quad (4)$$

In vivo human imaging. The imaging experiment in a healthy volunteer was performed in full accordance with work safety regulations of Helmholtz Zentrum München. The per-pulse energy and average power levels of the lasers conformed to standards for the safe use of lasers at all times²⁷. To avoid signal saturation due to strong photoacoustic responses from the surface, the hair in the imaged region was removed prior to the experiments using a shaving lotion. The hand-held probe was moved along the skin surface with scanning speeds ranging from 1 to 10 mm/s, as estimated in the post-processing step.

- Oraevsky, A. *et al.* Laser photoacoustic imaging of the breast: detection of cancer angiogenesis. *Proc. of SPIE*. **3597**, p. 352–363 (1999).
- Wang, X. D. *et al.* Noninvasive laser-induced photoacoustic tomography for structural and functional in vivo imaging of the brain. *Nat. Biotechnol.* **21**, 803–806 (2003).
- Tainter, C. S. & Bell, A. G. Selenium and the photophone. *Nature*. **22**, 500–503 (1880).
- Razansky, D., Buehler, A. & Ntziachristos, V. Volumetric real-time multispectral photoacoustic tomography of biomarkers. *Nat. protoc.* **6**, 1121–1129 (2011).
- Wang, L. H. V. & Hu, S. Photoacoustic Tomography: In Vivo Imaging from Organelles to Organs. *Science*. **335**, 1458–1462 (2012).
- Heijblom, M. *et al.* Visualizing breast cancer using the Twente photoacoustic mammoscope: What do we learn from twelve new patient measurements? *Opt. express*. **20**, 11582–11597 (2012).
- Kruger, R. A. *et al.* Dedicated 3D photoacoustic breast imaging. *Med. phys.* **40**, 113301 (2013).
- Razansky, D. *et al.* Multispectral Photoacoustic Tomography of Matrix Metalloproteinase Activity in Vulnerable Human Carotid Plaques. *Mol. Imaging Biol.* **14**, 277–285 (2012).
- Jiao, S. L. *et al.* Photoacoustic ophthalmoscopy for in vivo retinal imaging. *Opt. express*. **18**, 3967–3972 (2010).
- Sun, Y., Sobel, E. S. & Jiang, H. B. First assessment of three-dimensional quantitative photoacoustic tomography for in vivo detection of osteoarthritis in the finger joints. *Med. phys.* **38**, 4009–4017 (2011).
- Erpelding, T. N. *et al.* Sentinel Lymph Nodes in the Rat: Noninvasive Photoacoustic and US Imaging with a Clinical US System. *Radiology*. **256**, 102–110 (2010).
- Zhang, C., Maslov, K. & Wang, L. H. V. Subwavelength-resolution label-free photoacoustic microscopy of optical absorption in vivo. *Opt. Lett.* **35**, 3195–3197 (2010).
- Wang, X. D., Roberts, W. W., Carson, P. L., Wood, D. P. & Fowlkes, J. B. Photoacoustic tomography: a potential new tool for prostate cancer. *Biom. opt. express*. **1**, 1117–1126 (2010).
- Levi, J. *et al.* Molecular photoacoustic imaging of follicular thyroid carcinoma. *Clin. Cancer Res.* **19**, 1494–1502 (2013).
- Buehler, A., Kacprowicz, M., Taruttis, A. & Ntziachristos, V. Real-time handheld multispectral photoacoustic imaging. *Opt. Lett.* **38**, 1404–1406 (2013).
- Dean-Ben, X. L. & Razansky, D. Functional photoacoustic human angiography with handheld video rate three dimensional scanner. *Photoacoustics* **1**, 68–73 (2013).
- Buehler, A., Dean-Ben, X. L., Claussen, J., Ntziachristos, V. & Razansky, D. Three-dimensional photoacoustic tomography at video rate. *Opt. express*. **20**, 22712–22719 (2012).
- Xiang, L. Z., Wang, B., Ji, L. J. & Jiang, H. B. 4-D Photoacoustic Tomography. *Sci. Rep.-Uk*. **3**, 1113 (2013).
- Dean-Ben, X. L., Ozbek, A. & Razansky, D. Volumetric Real-Time Tracking of Peripheral Human Vasculature With GPU-Accelerated Three-Dimensional Photoacoustic Tomography. *IEEE T. med. imaging*. **32**, 2050–2055 (2013).
- Kim, C., Favazza, C. & Wang, L. V. In vivo photoacoustic tomography of chemicals: high-resolution functional and molecular optical imaging at new depths. *Chem. rev.* **110**, 2756–2782 (2010).
- Razansky, D. Multi-Spectral Photoacoustic Tomography – Volumetric Color Hearing in Real Time. *IEEE J. Sel. Top. Quant.* **18**, 1234–1243 (2012).
- Yang, J. M. *et al.* Simultaneous functional photoacoustic and ultrasonic endoscopy of internal organs in vivo. *Nat. med.* **18**, 1297–1302 (2012).
- Wang, L., Maslov, K. & Wang, L. V. Single-cell label-free photoacoustic flowoxigraphy in vivo. *P. Natl. Acad. Sci. USA*. **110**, 5759–5764 (2013).
- Wang, L. D., Maslov, K., Xing, W. X., Garcia-Urbe, A. & Wang, L. H. V. Video-rate functional photoacoustic microscopy at depths. *J. biomed. opt.* **17**, 106007 (2012).
- Dean-Ben, X. L. & Razansky, D. Adding fifth dimension to photoacoustic imaging: volumetric time-resolved spectrally-enriched tomography. *Light: Science & Applications*. **3**, e137 (2014).
- Dean-Ben, X. L. & Razansky, D. Portable spherical array probe for volumetric real-time photoacoustic imaging at centimeter-scale depths. *Opt. express*. **21**, 28062–28071 (2013).
- American National Standards for the Safe Use of Lasers ANSI Z136.1. American Laser Institute. 2000.
- Allen, T. J. & Beard, P. C. Pulsed near-infrared laser diode excitation system for biomedical photoacoustic imaging. *Opt. Lett.* **31**, 3462–3464 (2006).
- Kolkman, R. G. M., Steenbergen, W. & van Leeuwen, T. G. In vivo photoacoustic imaging of blood vessels with a pulsed laser diode. *Laser. Med. Sci.* **21**, 134–139 (2006).
- Lutzwieiler, C. & Razansky, D. Photoacoustic imaging and tomography: reconstruction approaches and outstanding challenges in image performance and quantification. *Sensors* **13**, 7345–7384 (2013).
- Dean-Ben, X. L., Buehler, A., Ntziachristos, V. & Razansky, D. Accurate model-based reconstruction algorithm for three-dimensional photoacoustic tomography. *IEEE Transactions on Medical Imaging*. **31**(10):1922–28 (2012).
- Razansky, D. *et al.* Multispectral photoacoustic tomography of deep-seated fluorescent proteins in vivo. *Nat. Photonics*. **3**, 412–417 (2009).
- Hochuli, R., Beard, P. C. & Cox, B. Accuracy of approximate inversion schemes in quantitative photoacoustic imaging. *Proc. of SPIE*. **8943**, p. 89435V (2014).
- Jacques, S. L. Optical properties of biological tissues: a review. *Phys. med. biol.* **58**, R37–R61 (2013).

Acknowledgments

The research leading to these results received funding from the European Research Council under grant agreement ERC-2010-StG-260991. The authors acknowledge the valuable inputs from G. Pang and S.J. Ford.

Author contributions

X.L.D.B. designed and performed the experiments, analyzed the data and wrote the manuscript. E.B. performed the experiments, discussed the results and wrote the manuscript. D.R. designed the experiments, discussed the results, wrote the manuscript and supervised the project.

Additional information

Supplementary information accompanies this paper at <http://www.nature.com/scientificreports>



Competing financial interests: The authors declare no competing financial interests.

How to cite this article: Deán-Ben, X.L., Bay, E. & Razansky, D. Functional optoacoustic imaging of moving objects using microsecond-delay acquisition of multispectral three-dimensional tomographic data. *Sci. Rep.* **4**, 5878; DOI:10.1038/srep05878 (2014).



This work is licensed under a Creative Commons Attribution-NonCommercial-NoDerivs 4.0 International License. The images or other third party material in

this article are included in the article's Creative Commons license, unless indicated otherwise in the credit line; if the material is not included under the Creative Commons license, users will need to obtain permission from the license holder in order to reproduce the material. To view a copy of this license, visit <http://creativecommons.org/licenses/by-nc-nd/4.0/>